

3D structure of the H II region Sh2-235 from tunable-filter optical observations

M. S. Kirsanova,^{1,2★} P. A. Boley^{2,3}, A. V. Moiseev⁴, D. S. Wiebe¹, R. I. Uklein⁴

¹*Institute of Astronomy, Russian Academy of Sciences, 119017, 48 Pyatnitskaya Str., Moscow, Russia*

²*Moscow Institute of Physics and Technology, 141701, 9 Institutskiy per., Dolgoprudny, Moscow Region, Russia*

³*Institute of Natural Sciences and Mathematics, Ural Federal University, 19 Mira Str., 620075 Ekaterinburg, Russia*

⁴*Special Astrophysical Observatory, Russian Academy of Sciences, Nizhny Arkhyz 369167, Russia*

Accepted 2020 July 04. Received 2020 July 04; in original form 2019 November 11

ABSTRACT

We present observations of the H α , H β , [S II] $\lambda\lambda 6716, 6731$ and [N II] $\lambda 6583$ emission lines in the galactic H II region Sh2-235 with the Mapper of Narrow Galaxy Lines (MaNGaL), a tunable filter at the 1-m telescope of the Special Astrophysical Observatory of the Russian Academy of Sciences. We show that the H II region is obscured by neutral material with $A_V \approx 2 - 4$ mag. The area with the highest A_V is situated to the south-west from the ionizing star and coincides with a maximum detected electron density of $\gtrsim 300 \text{ cm}^{-3}$. The combination of these results with archive *AKARI* far-infrared data allows us to estimate the contribution of the front and rear walls to the total column density of neutral material in S235, and explain the three-dimensional structure of the region. The H II region consist of a denser, more compact portion deeply embedded in the neutral medium and the less dense and obscured gas. The front and rear walls of the H II region are inhomogeneous, with the material in the rear wall having a higher column density. We find a two-sided photodissociation region in the dense clump S235 East 1, illuminated by a UV field with $G_0 = 50 - 70$ and 200 Habing units in the western and eastern parts, respectively.

Key words: ISM: HII regions — ISM: dust, extinction — ISM: photodissociation region (PDR) — stars: massive — techniques: imaging spectroscopy

1 INTRODUCTION

The H II region Sh2-235 (S235 hereafter, [Sharpless 1959](#)) is the brightest H II region among four close emission nebulae (the others being Sh2-231, Sh2-232 and Sh2-233) located in the giant molecular cloud G174+2.5 ([Ladeyschikov et al. 2016](#)) in the direction of the Aur OB1 association ([Straizys et al. 2010](#)) in the Perseus Spiral Arm. S235 and its surroundings are a region of active star formation (see e.g. recent studies by [Chavarría et al. 2014](#); [Bieging et al. 2016](#)). It contains at least five young stellar clusters projected on the border of the H II region, as was initially shown by [Kirsanova et al. \(2008\)](#), and later studied by [Camargo et al. \(2011\)](#); [Dewangan & Anandarao \(2011\)](#); [Kirsanova et al. \(2014\)](#). The surroundings of S235, namely the photodissociation region (PDR), molecular envelope, and young stellar objects embedded in the envelope, have been extensively observed at infrared ([Allen et al. 2005](#); [Klein et al. 2005](#); [Anderson et al. 2019](#)) and radio wavelengths ([Israel & Felli 1978](#); [Sil-](#)

[verglate & Terzian 1978](#); [Evans & Blair 1981](#); [Lafon et al. 1983](#); [Heyer et al. 1996](#); [Kirsanova et al. 2014](#); [Bieging et al. 2016](#); [Ladeyschikov et al. 2016](#); [Burns et al. 2019](#)), although the H II region itself has not been extensively studied.

Using radio recombination line (RRL) emission, [Quireza et al. \(2006a,b\)](#) determined that S235 (their source G173.60+2.80) has a nearly circular shape with an angular diameter of about $5'$, an electron density of $n_e = 81.6 \text{ cm}^{-3}$ and an electron temperature of $T_e = 8940 \pm 170 \text{ K}$. [Anderson et al. \(2019\)](#), using a combination of carbon and hydrogen RRLs, [C II] emission at $158 \mu\text{m}$ and CO emission determined that the H II region lies on the near side of the associated molecular cloud and is expanding in the direction of the observer. The distance to the ionizing star of S235, BD+35°1201, is $1.65 \pm 0.1 \text{ kpc}$, based on the Gaia DR2 parallax measurements ([Gaia Collaboration et al. 2016, 2018](#)) and the distance calibration of [Bailer-Jones et al. \(2018\)](#). The H II region is excited by a late O- ([Georgelin et al. 1973](#)) or early B-type ([Hunter & Massey 1990](#)) star. [Lafon et al. \(1983\)](#) inspected an H α image of the nebula, and found that it consists of a bright northern, and more diffuse southern,

★ E-mail: kirsanova@inasan.ru

part. They also reported a north-south radial velocity gradient of the ionized gas, although this was not confirmed by recent observations of RRLs by [Anderson et al. \(2019\)](#). [Straizys et al. \(2010\)](#) determined the interstellar extinction towards the ionizing star to be $A_V = 3.7$ mag. [Esteban & García-Rojas \(2018\)](#) measured the physical parameters of the nebula with optical slit spectroscopy, and found $n_e = 120 \text{ cm}^{-3}$ from the $[\text{S II}] \lambda\lambda 6716, 6731$ lines and T_e in the range from 7100 to 11900 K, depending on the line ratio used ($[\text{N II}]$, $[\text{S II}]$, $[\text{O II}]$ or $[\text{O III}]$ lines). These optical observations were confined to a single slit position with a length of $30''$, and therefore do not give a full overview of the properties of the ionized gas in this extended H II region.

The aim of the present work is to study the properties and spatial distribution of the ionized gas in S235 using narrow-band images in optical forbidden and Balmer emission lines, obtained with a new tunable-filter photometer at the 1-m Zeiss-1000 telescope of the Special Astrophysical Observatory of the Russian Academy of Sciences (SAO RAS), supplemented by additional imaging and spectroscopic data from space- and ground-based telescopes (AKARI infrared imaging satellite, SAO RAS 6-m telescope, and previously published CO maps).

2 OBSERVATIONS AND DATA REDUCTION

2.1 MaNGaL imaging

We performed observations using the Zeiss-1000 telescope of SAO RAS with the Mapper of Narrow Galaxy Lines (MaNGaL). MaNGaL is a new tunable-filter photometer developed at SAO RAS, based on a piezoelectric scanning Fabry-Perot interferometer (FPI) with low interference order ($n \approx 20$ in the $\text{H}\alpha$ line). The instrument was described by [Moiseev et al. \(2020\)](#) and at the SAO RAS web-page¹. First results using the instrument were presented by [Keel et al. \(2019\)](#). The width of the instrumental profile in the spectral range used was $\text{FWHM} = 14 \pm 1 \text{ \AA}$, and the central wavelength (CWL) of the peak of FPI transmission was precisely tuned to the desired wavelength (better than 0.5 \AA) at the centre of the field of view. For the observations in January 2018 we used an Andor iKON-M 934 CCD Camera, which provides a field of view of $8.7''$ and a plate scale $0.51''/\text{px}$.

Unlike the ‘classical’ optical layout having a tunable filter in the collimated beam (e.g. [Jones et al. 2002](#)), MaNGaL is an afocal reducer with the FPI in the convergent beam ([Courtes 1960](#)). This arrangement provides a significantly larger field for the central monochromatic region (‘Jacquinot spot’), which is crucial for studying extended targets. In our case, CWL varies with a range smaller than the filter $\pm 0.5 \text{ FWHM}$ across the whole field of view. As a result, variations of the FPI transmission of the nebular emission lines in S235 should not be very significant, because their line-of-sight velocity variations are smaller than 100 km s^{-1} (Sec. 2.2). Nevertheless, we applied a correction for the effects of CWL variations (see below).

We show the observation log of the MaNGaL observations in Table 1, where the seeing is given for the resulting

combination of all frames. The most deep and detailed data in the $\text{H}\alpha$ and $[\text{S II}]$ lines were obtained in January, 2018, in the ‘single images FPI mode’, where the CWL is tuned first to the emission line (taking into account the systemic velocity of the target and heliocentric correction), and then to the neighbouring continuum (shifted by $30 - 50 \text{ \AA}$). This cycle was repeated, which averages the contribution of atmospheric seeing and variations in atmospheric transparency. The FPI transmission peaks from neighbouring interference orders were fully blocked using medium-width filters with a bandwidth of $\sim 250 \text{ \AA}$. Different blocking filters were used for $\text{H}\alpha$ and $[\text{S II}]$ spectral ranges. In the case of the $[\text{S II}]$ doublet, the continuum was observed both redward and blueward of the emission lines; for $\text{H}\alpha$, the continuum was observed only on the blue side.

In order to understand how these single images were affected by the mismatch between the FPI peak CWL and the emission line centre, immediately after taking deep images we performed observations in the ‘scanning FPI mode’; i.e. we quickly scanned the wavelength regions around the $\text{H}\alpha + [\text{N II}]$ and $[\text{S II}]$ emission lines: 12 subsequent frames with CWL increments of 7.5 \AA were obtained for each spectral interval with relatively short (60 s) exposures, to minimize the effects of atmospheric variations. The CCD was operated with 4×4 binning in order to obtain a signal-to-noise (S/N) ratio comparable to that of the single images.

In September 2018, we used an Andor Neo 5.5 sCMOS camera, because the primary CCD detector was under repair. With 2×2 binning the Neo sCMOS provides the same sampling ($0.5''/\text{px}$) and field of view, but with lower quantum efficiency and significantly higher noise compared to the iKON CCD. For these observations MaNGaL was operated in the ‘direct images mode’ like a standard photometer, without the FPI. Images were exposed in medium-band filters with $\text{FWHM} \sim 100 \text{ \AA}$ centred on the $\text{H}\beta$ emission line (filter CWL $\approx 4880 \text{ \AA}$) and continuum near (CWL $\approx 5150 \text{ \AA}$).

The data reduction was performed using a custom software package running in the IDL environment², which includes bias (for CCD) and dark current (for sCMOS) subtraction, flat-field correction, and cosmic ray removal by combining individual short exposures at the same wavelength. Continuum emission was removed from the images in the lines by normalising the continuum to minimise the flux residuals in the background and foreground stars. Per-pixel uncertainties were derived based on photon statistics in the line and continuum images. The typical value of the background RMS of the net emission line images was $(3-6) \times 10^{-17} \text{ ergs cm}^{-2} \text{ sec}^{-1} \text{ arcsec}^{-2}$. The quality of the continuum subtraction in the single images obtained with the FPI mode was significantly better than in those obtained in the ‘classical’ filter direct images in $\text{H}\beta$, due to the fact that the continuum was observed at very close wavelengths and with a much narrower filter width.

In order to calibrate the images to an absolute intensity scale, each night we observed spectrophotometric standard stars in the corresponding observing mode immediately before or after S235, and at a similar airmass. In January, 2018 we observed the standard star G191B2B at a zenith

¹ https://www.sao.ru/Doc-en/Events/2017/Moiseev/moiseev_eng.html

² <https://www.harrisgeospatial.com/Software-Technology/IDL>

distance of $z = 25^\circ$, which corresponds to an airmass of 1.10, whereas S235 was observed in the airmass range 1.04–1.19. In September, 2018 the nebula was observed in the larger airmass range 1.05–1.66, while the standard stars H α and H β were exposed at zenith distances corresponding to airmasses of 1.04, 1.16 and 1.74. All nights were photometric. The equations from Jones et al. (2002) were used for calibration of our tunable-filter data. The SAO RAS extinction curve (Kartasheva & Chunakova 1978) was used for atmospheric extinction correction. The difference between the S235 H β fluxes estimated in different nights in September, 2018 was about 4%. This value can be considered as the accuracy of our flux calibration.

The astrometric calibration was performed using astrometry.net (Lang et al. 2010) and index files compiled from the Gaia DR2 catalog (Gaia Collaboration et al. 2018). Using 56 Gaia stars in the field brighter than $G = 17$ mag, we find a position RMS of the astrometric solution of $0.12''$.

For the wavelength calibration and analysis of the images obtained in the scanning mode, we modified the IDL-based software for scanning FPI data reduction of Moiseev & Egorov (2008). The images were merged into data cubes containing a 12-channel spectrum at each pixel. These low-resolution spectra were fitted at each position in the field by a combination of Gaussians, corresponding to the H α , [N II] $\lambda\lambda 6548, 6583$ and [S II] $\lambda\lambda 6716, 6731$ emission lines. The wavelength difference between lines, $FWHM$ and [N II] doublet ratio (1:3) were fixed, while the radial velocity and line amplitudes were left as free parameters. After this procedure we have two types of 4×4 binning maps in the H α and [S II] lines: (1) the fitting results (F_{fit}), free from CWL -emission peak mismatch; (2) the data cube channels (F_{image}) observed with the same parameters of the FPI as the corresponding ‘single images’. The ratio of $F_{\text{fit}}/F_{\text{image}}$ after smoothing and interpolation was used to correct the emission line images in the original 1×1 binning resolution. In most areas of the field the correction is negligible ($F_{\text{fit}}/F_{\text{image}} = 0.95 - 1.1$), and it exceeded a factor of 1.2 only in the northwest edge of the field, where a small emission filament is located. The uncertainty of this ratio estimated as an RMS value on the non-smoothed maps was 0.03–0.05 in the main field, and about 0.1–0.2 at the northwest edge of the nebula.

This type of correction only affects the absolute flux distribution and H β /H α ratio, and does not affect the line ratio maps taken in the ‘single images’ mode: [S II]/H α , [S II] $\lambda 6716$ /[S II] $\lambda 6731$. As a side result, the data cube fitting also provided an emission map of the [N II] $\lambda 6583$ line.

2.2 SCORPIO-2 spectroscopy

In order to check the calibration of the line flux ratios measured by MaNGaL, we used two medium-resolution ($FWHM \sim 4.5 \text{ \AA}$) slit spectra presented by Boley et al. (in prep.), obtained with the SCORPIO-2 instrument (Afanasyev & Moiseev 2011) on the 6-m BTA telescope of SAO RAS in February, 2019. The spectra cover two portions of the S235 nebula along the $6'$ slit, illustrated in Fig. 1, and the H α , H β , [S II] 6716, 6731 \AA lines are spectrally resolved, with an estimated absolute flux calibration accurate to about 5%. We refer to the work of Boley et al. for a full description of these observations and their reduction.

For each wavelength observed with MaNGaL, we

Table 1. MaNGaL observations at the SAO RAS Zeiss-1000 telescope

Date	Sp. range	Exposure, s	seeing, ''
<i>Mode: single images with FPI</i>			
2018 Jan 26	H α	1200	1.9
	H α continuum	1200	1.9
	[S II] $\lambda 6716$	2700	1.9
	[S II] $\lambda 6731$	5400	1.9
	[S II] continuum 1	2700	1.9
	[S II] continuum 2	2700	1.9
<i>Mode: scanning with FPI</i>			
2018 Jan 26	H α + [N II]	12×60	1.9
2018 Jan 26	[S II]	12×60	1.9
<i>Mode: direct images</i>			
2018 Sep 18	H β	4800	2.5
	H β continuum	5400	2.5
2018 Sep 19	H β	5100	1.9
	H β continuum	3900	1.9
2018 Sep 20	H β	6600	1.6
	H β continuum	6600	1.6

matched the spatial resolution of the images ($2.1''$) to that of the SCORPIO-2 spectra ($2.6''$) by simple Gaussian convolution. Next, we created spatial profiles of the emission in each line from the MaNGaL observations by integrating along the width of the slit ($1''$) at each position along the length of the SCORPIO-2 slit. Finally, because of the lower SNR in the slit spectra of the fainter regions of the nebula, we applied 9-pixel ($3.1''$) boxcar smoothing to the spatial profiles (from both MaNGaL and SCORPIO-2).

3 METHODS

3.1 Properties of the ionized gas

Electron density n_e was determined from the ratio of [S II] lines $\lambda 6716/\lambda 6731$. Because the wavelength difference between the doublet lines is comparable to the MaNGaL FPI instrumental profile, a correction must be applied. For a Lorentzian profile, which is a good approximation of FPI instrumental contour (Moiseev & Egorov 2008, and references therein), the real ratio r_{real} of two lines separated by $\Delta\lambda$ is related to the observed ratio r_{obs} by the relation

$$r_{\text{real}} = \frac{1 - C \cdot r_{\text{obs}}}{r_{\text{obs}} - C}, \quad (1)$$

where $C = 1 + \left(\frac{2\Delta\lambda}{FWHM}\right)^2$ characterises the Lorentzian profile.

The observed MaNGaL map of [S II] $\lambda 6716/\lambda 6731$ was corrected according to Eq. (1). Finally, we compared the spatial profiles of the [S II] line ratio along the SCORPIO-2 slit with the same locations in the MaNGaL data using the procedure described in Sec. 2.2. We found that the [S II] $\lambda 6716/\lambda 6731$ and H α /H β values measured by MaNGaL must be further multiplied by a constant factor of 1.186 and 0.798 respectively to bring them in line with the flux-calibrated slit spectra. This secondary correction may be due to several factors, including deviations of the real on-sky instrumental profile wings from the purely Lorentzian profile of the calibration lamp spectrum.

The value of n_e was then calculated at each pixel with S/N level > 3 from the corrected ratio of the [S II] lines using Eqs. (3) and (4) of Proxauf et al. (2014), for a mean electron temperature $T_e = 7280$ K (Boley et al., in prep). If the variations of electron temperature throughout the nebula are assumed to be on the order of ~ 170 K (Esteban & García-Rojas 2018, and references therein), the effect on the n_e values derived from the relations of Proxauf et al. (2014) are less than 2.5%. Therefore, we do not attempt to account for variations in T_e when considering trends in n_e throughout the nebula.

We determined the interstellar extinction A_V using the observed $H\alpha/H\beta$ intensity ratio and the intrinsic ratio for Case B conditions and the reddening law of Cardelli et al. (1989). By interpolating the values from Table 4.2 of Osterbrock & Ferland (2006) in log-log space for $T_e = 7280$ K, we find an intrinsic intensity ratio of $j_{H\alpha}/j_{H\beta} = 2.95$. For the ratio of total to selective extinction, we adopted a value of $R_V = 3.0$ (Boley et al., in prep.).

To study the geometry of the H II region, we estimate its depth along the line of sight (S) for the each pixel using equation:

$$S = \frac{4\pi I_{H\alpha}}{h\nu_{H\alpha}} \frac{1}{n_e n_{H^+} \alpha_2} \text{ cm}, \quad (2)$$

where $\alpha_2 = 3.94 \times 10^{-14} \text{ cm}^3 \text{ s}^{-1}$ is the Case B hydrogen recombination coefficient, interpolated for an electron temperature of $T_e = 7280$ K (Table 4.2, Osterbrock & Ferland 2006), $I_{H\alpha}$ is from original calibrated MaNGAL files in $\text{ergs cm}^{-2} \text{sec}^{-1} \text{arcsec}^{-2}$ transferred to $\text{ergs cm}^{-2} \text{sec}^{-1} \text{sr}^{-1}$. We assume that the physical conditions (n_e and T_e) do not vary over the line of sight, and ignore the ionization of all atoms other than hydrogen, i.e. $n_e = n_{H^+}$. While the physical conditions might not be truly uniform along the line of sight, we find below that the derived values of S are reasonable and consistent with the overall structure of the H II region seen in the distribution of A_V and n_e . Regarding the ionization conditions, the abundance of ionized helium, which produces additional free electrons in the H II region, is about 100 times less than that of H^+ . The abundance of other ionized elements is even smaller.

3.2 Dust temperature and column density

In order to estimate dust temperature and column density, we used far-infrared emission maps at 90, 140, and 160 μm (WIDE-S, WIDE-L and N160 bands, respectively, Kawada et al. 2007), collected by the Far-Infrared Surveyor (FIS) instrument on the AKARI satellite (Murakami et al. 2007; Kaneda et al. 2007) during the AKARI Far-infrared All-Sky Survey (Doi et al. 2015; Takita et al. 2015). According to Kawada et al. (2007), the average spatial resolution (FWHM) of the instrument at the IR bands listed above is 39, 58, and 61'', respectively. Later measurements produced somewhat greater FWHM values and revealed the elliptical shape of the PSF, which is more elongated at shorter wavelengths (Takita et al. 2015; Ueta et al. 2019). According to Ueta et al. (2019), the in-scan FWHMs are $103.8 \pm 5.1''$, $104.2 \pm 7.9''$, and $85.5 \pm 8.3''$ for 90, 140, and 160 μm , respectively, while the cross-scan FWHMs for these same wavelengths are $68.5 \pm 3.1''$, $77.9 \pm 7.0''$, and $73.3 \pm 5.8''$. Based on these estimates, we conclude that the spatial resolutions

of the maps at the wavelengths used are similar, so we have not attempted to convolve them to the same resolution. Dust temperatures and column densities were computed with the modified black body approach, adopting $\beta = -1.59$ and an opacity at 850 μm of $0.5 \text{ cm}^2 \text{ g}^{-1}$ (Planck Collaboration et al. 2014).

We downloaded the AKARI data from the IRSA archive³ and regridded them to the astrometric grid of the 90 μm image with a pixel size of 15''. We used the standard HASTROM IDL procedure⁴ with the default bilinear interpolation. Dust temperatures and column densities were computed with the modified black body approach, adopting various prescriptions for dust opacities (see below). Having obtained the dust temperature T_{dust} from the SED fitting, we applied the general approach described by Hildebrand (1983) and used a standard dust-to-gas mass ratio 1/100 to obtain the hydrogen column density map.

To estimate the radiation field in units of the Habing field (G_0 Habing 1968), we use equation (5.44) from Tielens (2005) for a grain radius of 0.1 μm :

$$T_{\text{sil}} \approx 50 \left(\frac{1\mu\text{m}}{a} \right)^{0.06} \left(\frac{G_0}{10^4} \right)^{1/6}. \quad (3)$$

We use 0.1 μm as a reference size of a typical interstellar grain. This choice is motivated the fact that the peak of the grain size distribution is close to 0.1–0.3 μm (e. g. Weingartner & Draine 2001). Additionally, the interstellar grain size distribution, recalculated in terms of mass fraction, has a peak near 0.1 μm (Kim et al. 1994).

4 RESULTS OF THE OBSERVATIONS WITH MANGAL

Images of the emission in the $H\alpha$, $H\beta$, [S II], and [N II] lines are shown in Fig. 1. Only pixels with S/N higher than 3 are shown. In Appendix A (supplementary material available online) we show the maps of signal to noise ratios for each. The images of $H\alpha$ and $H\beta$ show a bright central part ('main' part) around the ionizing star, with a sharp edge to the north and west, and diffuse emission to the south. The peaks of the $H\alpha$ and $H\beta$ emission are about 60'' to the north-east of the ionizing star (0.5 pc in the plane of the sky). The area of the brightest $H\alpha$ and $H\beta$ emission is marginally coincident with the 1.4 GHz radio emission peak. The radio continuum emission is also present in the diffuse, southern part of the optical nebula.

In contrast to the bright $H\alpha$ emission, [S II] lines were only detected in the main part of the nebula with S/N > 3 . The peak of the [S II] emission is coincident with the peak of $H\alpha$ and $H\beta$ emission. Several arc-like filaments are visible in the [S II] maps to the north-east from the ionizing star. There is also a bright, separated filamentary structure in the north-west part of the main nebula detected in all five lines.

In Fig. 2, we show the spatial distribution of n_e throughout the nebula. As we are interested in large-scale trends, and in order to increase the S/N ratio, the images were rebinned to a pixel size 16 times larger (8.1'') than the original

³ <https://irsa.ipac.caltech.edu>

⁴ <https://idlastro.gsfc.nasa.gov>

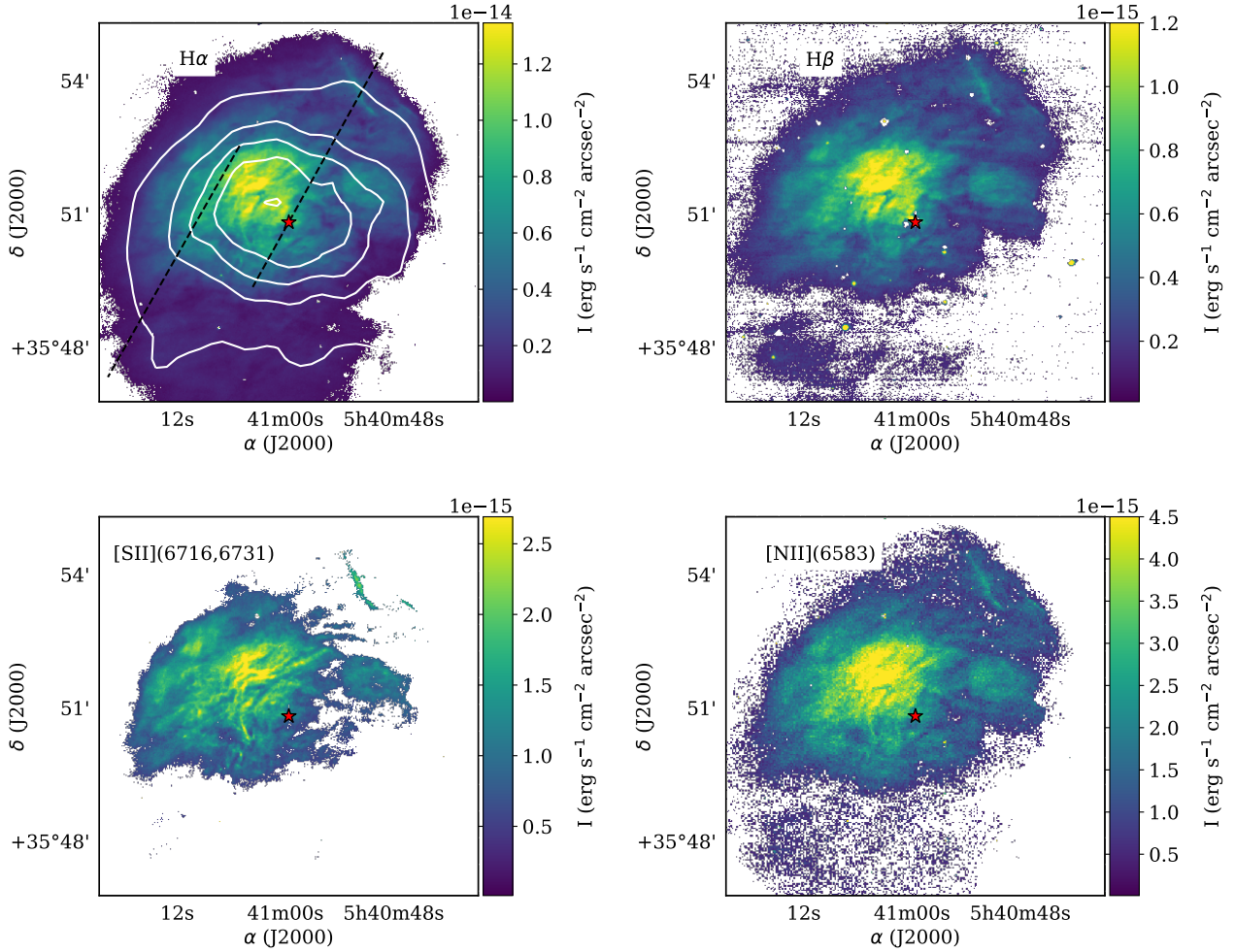


Figure 1. MaNGaL images of S235. Only pixels with S/N ratio > 3 are shown here. The NVSS 1.4 GHz image of S235 (Condon et al. 1998) is superimposed on the H α image with white contours, which are evenly spaced from 2.25 mJy/beam (5σ level) to 123 mJy/beam, and the dashed lines show the slit positions of the SCORPIO-2 spectra. The location of the ionizing star is shown in each frame as a red star.

pixel shown in Fig. 1. We show the resulting S/N ratio of the n_e distribution after this procedure in Appendix A. We find a density gradient from the north-east to the south-west part of the nebula, from $\sim 20 - 30$ cm $^{-3}$ to more than 300 cm $^{-3}$, with a median value of 96 cm $^{-3}$. We show a north-east/south-west spatial cut of the n_e value and its uncertainty in Fig. 3. Both n_e value and its uncertainty grow to the south-west. The gap in the cut at the position of the ionizing star is due to artefacts remaining from subtracting the bright stellar continuum at this location. The ionizing star is projected onto a region with $n_e > 150$ cm $^{-3}$. Due to the faintness of the [SII] lines in the south and south-west regions, the value of n_e is determined with greater uncertainty, and at some locations cannot be determined at all. The bright north-west filament visible in Fig. 1 is not distinguishable on the n_e map.

We performed a visual comparison of the n_e map from Fig. 2 with the spatial distribution of hydrogen and carbon radio recombination lines (RRLs and CRRLs, respectively) given by Anderson et al. (2019), shown in their Fig. 7. Due to the square-root dependence on density, the RRLs are the

best tracers of n_e in the HII region, but CRRLs trace n_e in the surrounding PDR. We see that the peak of the RRL emission corresponds to the direction of the ionizing star, but the peak of the CRRL emission is shifted to the south-west of the star and coincides with the region of the maximum A_V found with MaNGaL. Hence, the densest part of the HII region is adjacent to the densest part of the PDR around S235.

The spatial distribution of the optical extinction, expressed in terms of A_V , is also non-uniform in S235 (see Fig. 2). There is a gradient from $A_V = 1.5 - 2$ mag in the north-east part of the nebula to $A_V > 4$ mag in the south-west part. The A_V value in the direction of the ionizing star is ≈ 4 mag, consistent with the value found by Straizys et al. (2010). The typical uncertainty of the A_V value, which we calculated using a bootstrapping procedure by varying the H α and H β intensities within their respective uncertainties, is about 0.2 mag, which is less than 6% of the minimum A_V value found in the north-west part of the nebula. The map of the signal to noise ratio for A_V is shown in Appendix A. Comparing the n_e and A_V maps, we find that the direction

of the gradients is approximately the same, with higher n_e corresponding to higher A_V . The ionizing star is projected on the transitional region between the dense part of the H II region more deeply embedded in the surrounding neutral material and the more rarefied part. The transition from the less-dense and less-obscured part of the H II region to the denser part is visible in Fig. 3. The physical properties, as well as their uncertainties, change when crossing the star position.

The dereddened and rebinned H α image is shown in Fig. 2. After accounting for the foreground reddening, it can be seen that maximum of the H α emission coincides with the maximum of the 1.4 GHz NVSS image. The uncertainty of the dereddened H α flux reaches 50% in the south-west part of the nebula, where the A_V value is highest, but not more than 10–20% in other parts of the nebula.

We evaluated the extent of the H II region along the line of sight S using Eq. (2) and the distribution of the n_e value, and found that it varies within the range of $2 < S < 20$ pc in S235. The linear size of the nebula in the plane of the sky, corresponding to $5'$ at 1.65 kpc, is 2.4 pc. Thus, according to the optical data, the nebula is more extended along the line of sight. If we use the emission measure from the radio recombination lines of $EM = 3.7 \cdot 10^4$ pc cm $^{-6}$ (Silverglate & Terzian 1978) with the median value of n_e , we obtain 4.0 pc; i.e. our estimate of the extent from the optical recombination lines is in agreement with the radio-based value within a factor of 2–5, depending on the position in the nebula.

The value of S shows a gradient opposite in sign compared with both the n_e and A_V gradients, i.e. it increases from the south-west to north-east. The depth is about 2–7 pc at the location of the central star. Therefore, there is a more or less spherical/ellipsoidal volume of ionized gas to the south-west of the star. In the north-east part of the nebula, we find gas that is less dense, less obscured, and more extended along the line of sight. This region represents a location where the gas can more easily expand from the H II region into the direction of the observer. Indeed, Anderson et al. (2019) also showed a difference between the radial velocities of the hydrogen and carbon RRLs (–23 and –20 km s $^{-1}$, respectively) accompanying the expansion.

5 ANALYSIS OF DUST EMISSION

There are three different types of column density indicators which can be applied to this region. One is A_V derived from the Hydrogen Balmer lines in our MaNGaL observations. Another, A_V^{IR} , may be obtained from spectral fitting of the dust continuum emission, as described in Sec. 3.2 (see also Fig. 4, top). Finally, A_V^{CO} may be derived from the CO observations of Bieging et al. (2016), assuming a standard LTE approximation (Mangum & Shirley 2015) and relative abundance for CO of $1.2 \cdot 10^{-4}$ (see, for example, the work by Wakelam & Herbst (2008); this value is also in agreement with the latest calculation of carbon abundance in the region made with the CO, C $^+$ and $^{13}\text{C}^+$ lines by Kirsanova et al., in prep.). In a simple spherical-shell approximation, and for a line of sight passing through the shell centre, the first value (A_V) contains contributions from the ionized region and the front wall. The second value (A_V^{IR}) also contains contributions from the ionized region, as well as from both

the front and rear walls. Finally, the third value (A_V^{CO}) is presumably sensitive to the (molecular) material contained in the front and rear walls.

In this picture, A_V^{IR} should be the largest (provided the dust temperature does not vary along the line of sight), which is indeed what we see in general. In the region observed with MaNGaL, the median extinction values are 2.7, 4.0, and 2.9 mag for A_V , A_V^{IR} , and A_V^{CO} , respectively. However, this relation breaks down significantly at certain locations. Specifically, $A_V^{\text{IR}} < A_V$ at nearly all locations to the north of the ionizing star. Also, as the observer looks through the dense molecular clump southward of the ionizing star, $A_V^{\text{IR}} < A_V^{\text{CO}}$. This behaviour is somewhat unexpected, and may be caused by the choice of the opacity prescription. The Planck-based opacity parameters that we have utilised are more appropriate for the diffuse medium, while the gas in the studied region has a much higher density. We also tried other opacity prescriptions (e.g. Ossenkopf & Henning 1994), and they do not improve the situation. The CO-based extinction is also somewhat uncertain, as its value scales linearly with the adopted CO abundance, and this value is also prone to some variations. Overall, we conclude that extinctions based on *AKARI* data, as well as the extinctions based on the CO data, are uncertain up to a factor of two, and should therefore be used as a relative measure of column density, rather than absolute. We note, however, that the estimated dust temperature does not depend strongly on the adopted opacity.

The A_V^{IR} varies from 2 mag to the north of the ionizing star BD+35°1201 within the H II region, to more than 10 mag in the densest regions, which coincide with the peaks of the CO(2–1) emission (Bieging et al. 2016). If we consider only the area outlined by the NVSS contours, we find that the column density traced by both A_V^{IR} and A_V^{CO} increase from north to south, so that the directions of their gradients are not the same as the direction of the A_V gradient estimated with the hydrogen recombination lines. This implies that the front and rear walls of neutral material of the H II region are inhomogeneous, and contain different amounts of absorbing material.

Comparing the extinction values from Figs. 2 (top right) and 4 (top), we find that while A_V^{IR} is about 1.5 times as high as A_V in the direction of BD+35°1201, the A_V value does not vary much as we look through the dense region with an embedded young stellar cluster (S235 Central; Kirsanova et al. 2008) to the south of the ionizing star, where A_V^{IR} is significantly higher than A_V . This implies that the cluster and the dense clump are situated in the rear wall of the H II region. This conclusion is in agreement with findings by Anderson et al. (2019), who compared the radial velocities of carbon and hydrogen RRLs with the velocities of molecular gas in the same region. They found that the ionized gas flows in the direction of the observer, and that the neutral material forms a semi-envelope around the H II region from the rear and two side walls. In the present study, we show that the H II region has an inhomogeneous front wall, with a smaller column of neutral material than the rear wall.

The dust temperature derived from the SEDs (Fig. 4, middle) represents the average value of T_{dust} along the line of sight and varies from 18 to 30 K across the face of the H II region and the surrounding PDR, with a minor peak to the south-east of the ionizing star. Comparison of the

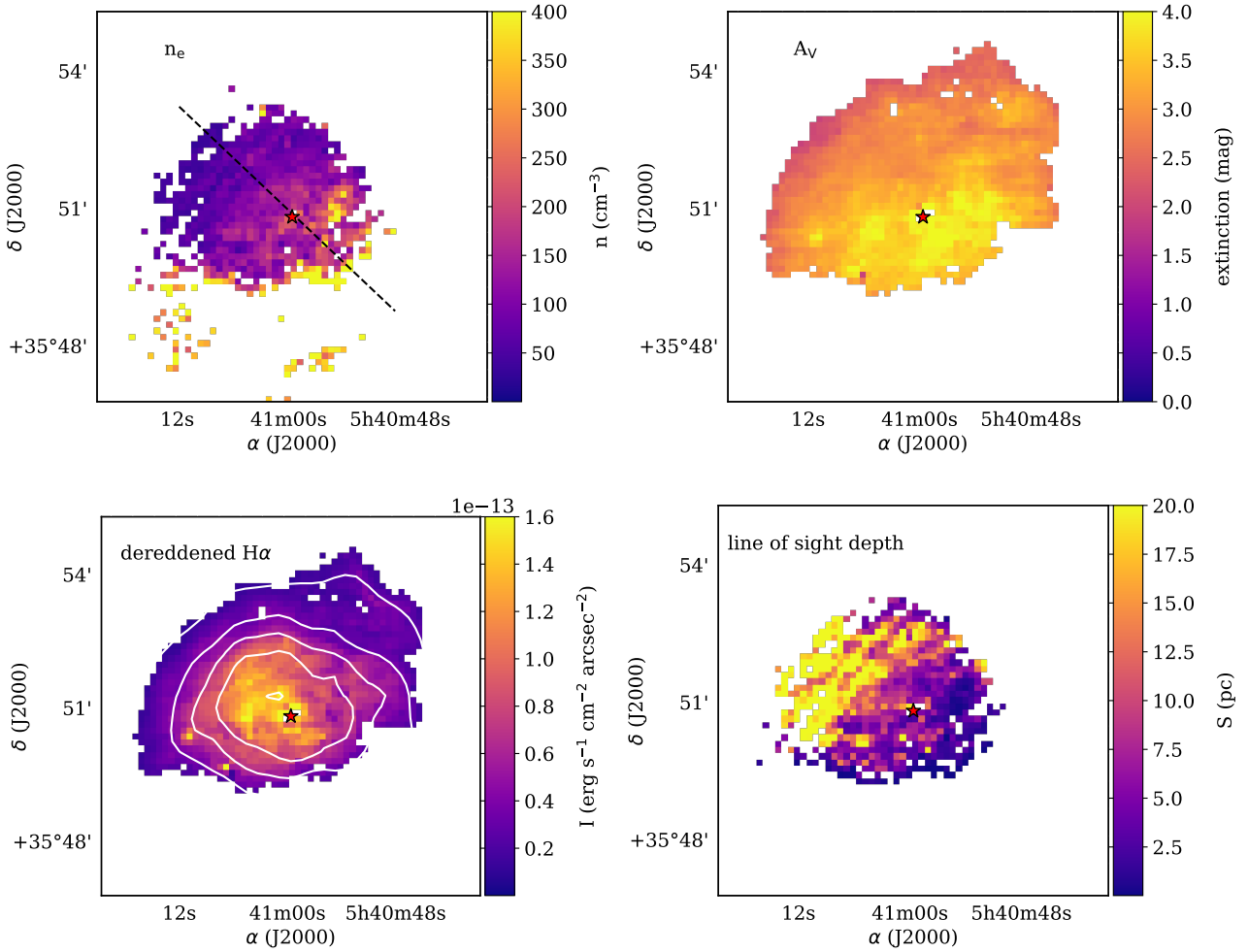


Figure 2. Rebinned electron density (top left) and A_V (top right), dereddened $H\alpha$ image (bottom left) and line-of-sight depth (bottom right) images of S235. Only pixels with S/N ratio > 3 are shown. The dashed line in the top left panel shows the location of the cut of the n_e value presented in Fig. 3.

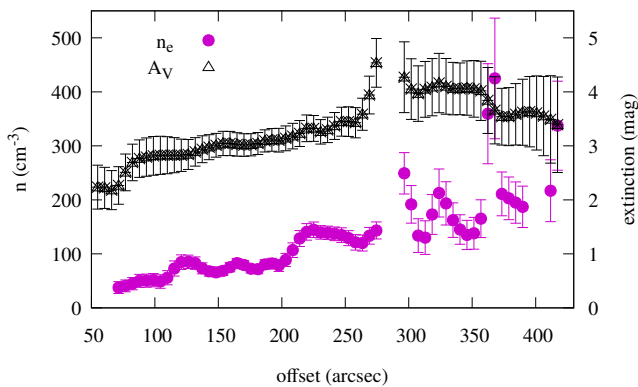


Figure 3. Cuts of n_e (violet circles) and A_V (black triangles) along the north-east/south-west direction. The position of the cut on the plane of the sky is shown in Fig. 2. The empty region on the cut corresponds to the position of the ionizing star and surrounding pixels.

CO(2–1) emission and corresponding $N(\text{H}_2)$ with the spatial distribution of the T_{dust} values shows that the peaks of the CO(2–1) in direction of the stellar clusters S235 East 1 and East 2 (Kirsanova et al. 2008) to the east of the H II region coincide with the regions with $T_{\text{dust}} < 20$ K. We do not find decreasing T_{dust} in the direction of S235 Central, probably due to the projection effect of the warm foreground dust heated by the BD+35°1201 star.

The typical value of FUV radiation field is $G_0 \approx 200$ in Habing units in the direction of the H II region (Fig. 4, bottom). The maximum value of G_0 does not correspond to the position of the ionizing star or to the bright infrared sources IRS 1 or IRS 2 found by Evans & Blair (1981), but rather with the local lows of the dust column density map to the north of the ionizing star, where the FUV emission is not absorbed by the dense neutral medium. The minimum FUV field in the direction of the S235 East 1 and East 2 clusters can be explained by the high gas density in the molecular clumps. The projected distance from the ionizing star to the western border of the dense gas ridges in the direction of the East 1 and East 2 clusters is $\approx 6'$, which corresponds to 2.8 pc. The value of G_0 is $\approx 30 - 50$ in the direction of the

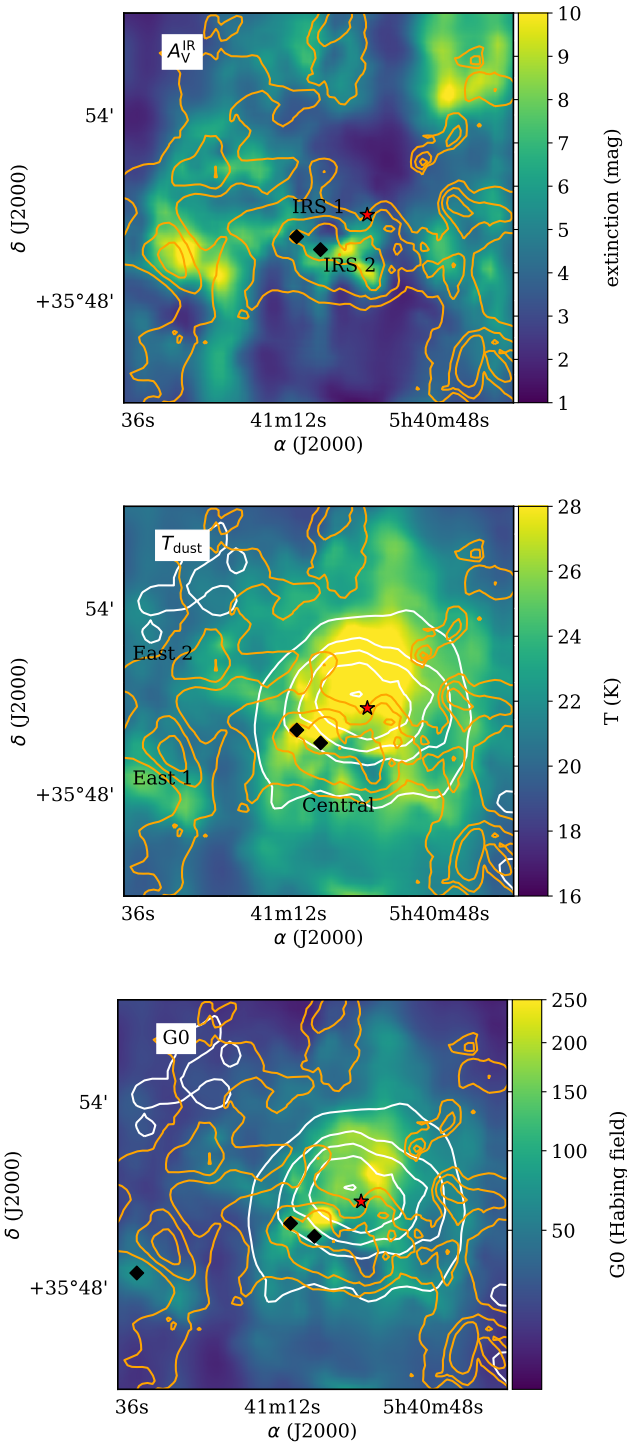


Figure 4. Top: dust extinction, middle: dust temperature, bottom: UV field in Habing units. NVSS radio continuum emission (Condon et al. 1998) is shown with white contours. The ionizing star is shown as the red star symbol, and the infrared sources IRS 1 and IRS 2 (Evans & Blair 1981) are shown as black diamonds. The map of $N(\text{H}_2)$ from Bieging et al. (2016) is shown with orange contours, and dense clumps with embedded young stellar clusters from Kirsanova et al. (2008) are designated. The contours, in terms of visual extinction, correspond to 5, 10 and 15 mag. The black diamond shown on the bottom panel indicates the position a possible illuminating source for S235 East 1 E PDR (see text).

western border of East 1 from the side of the ionizing star (S235 East 1 W below).

We find $G_0 \approx 100$, or 2-3 times higher, on the eastern border of East 1 (which we call S235 East 1 E below). The dense clump with the embedded cluster East 1 is probably irradiated from the east by another stellar source, visible, for example, on *WISE* or *Spitzer* images of the region at $\alpha(\text{J2000.0})=05^{\text{h}}41^{\text{m}}35.23^{\text{s}}$, $\delta(\text{J2000.0})=35^{\circ}48'27.5''$ (the source is shown in the bottom panel of Fig. 4). The value of G_0 here is comparable with the Horsehead PDR, where $G_0 \approx 100$ (Zhou et al. 1993). The gas number density in the S235 East 1 dense clump reaches up to $2 \times 10^4 \text{ cm}^{-3}$ based on measurements of NH_3 lines by Kirsanova et al. (2014). Thus, the dense clump S235 East 1 is a two-sided dense PDR with different G_0 values at each side, making this region an interesting target for studies of PDR chemistry.

6 CONCLUSIONS

We present the first observations of a galactic H II region with the optical tunable-filter photometer MaNGaL at the Zeiss-1000 telescope of SAO RAS. The observations were done in $\text{H}\alpha$, $\text{H}\beta$, two [SII] lines at $\lambda 6716, 6731 \text{ \AA}$ and the [NII] line at 6583 \AA . The distribution of absorbing material (in terms of A_V) was obtained using the $\text{H}\alpha$ and $\text{H}\beta$ images. The [SII] lines were used to obtain the value of n_e .

We conclude that optical emission of the H II region is attenuated by neutral material with $A_V \approx 2 - 4 \text{ mag}$ and a peak to the south-east from the ionizing star. The direction to the highest A_V coincides with the maximum detected electron density (up to $n_e > 300 \text{ cm}^{-3}$), with a median value 96 cm^{-3} .

The combination of the results of the optical observations with archive FIR data from the *AKARI* satellite allowed us to describe the 3D structure of the H II region: we obtain a contribution of the front and rear walls to the total column density of neutral material. We find that the rear wall of the H II region contains higher column of material than the front wall. This result agrees with recent study by Anderson et al. (2019), who found that the ionized gas of the H II region expands in the direction of the observer. The thick rear wall does not allow to the ionized gas to expand to the direction from the observer. The extent of the H II region along the line of sight varies from 2 pc in the south-west to more than 10 pc in the north-east direction.

We also estimated T_{dust} and the mean FUV field in terms of G_0 in S235 and the surrounding PDR, and found an interesting two-sided PDR in the dense clump S235 East 1, where $G_0 = 30 - 50$ and 100 in the western and eastern parts, respectively. This region is attractive for studies of dense PDR chemistry.

ACKNOWLEDGEMENTS

We thank the anonymous referee for critique and suggestions which led to the improvement of this manuscript. We are also thankful to O. V. Egorov for fruitful discussions, as well as D. V. Oparin and A. E. Perepelitsyn for their assistance in observations.

Data processing and analysis of the observational material by MSK and PAB was supported by the Russian Science Foundation, grant number 18-72-10132. The development of MaNGaL and the tunable-filter data reduction software were supported by the Russian Science Foundation, grant number 17-12-01335. This study is based on observations conducted with the 1-m and 6-m telescopes of the Special Astrophysical Observatory of the Russian Academy of Sciences, carried out with the financial support of the Ministry of Science and Higher Education of the Russian Federation (including agreement No. 05.619.21.0016, project ID RFMEFI61919X0016), and also on observations with AKARI, a JAXA project with the participation of ESA. This work made use of data from the European Space Agency (ESA) mission *Gaia* (<https://www.cosmos.esa.int/gaia>), processed by the *Gaia* Data Processing and Analysis Consortium (DPAC, <https://www.cosmos.esa.int/web/gaia/dpac/consortium>). Funding for the DPAC was provided by national institutions, in particular the institutions participating in the *Gaia* Multilateral Agreement. This research made use of NASA's Astrophysics Data System Bibliographic Services, SIMBAD database, operated at CDS, Strasbourg, France (Wenger et al. 2000), Astropy,⁵ a community-developed core Python package for Astronomy (Astropy Collaboration et al. 2013; Price-Whelan et al. 2018), Matplotlib (Hunter 2007) and APLpy, an open-source plotting package for Python Robitaille & Bressert (2012).

DATA AVAILABILITY

The data underlying this article are available in Zenodo, at <https://doi.org/10.5281/zenodo.3902074>.

REFERENCES

- Afanasiev V. L., Moiseev A. V., 2011, *Baltic Astronomy*, **20**, 363
- Allen L. E., Hora J. L., Megeath S. T., Deutsch L. K., Fazio G. G., Chavarría L., dell R. W., 2005, in Cesaroni R., Felli M., Churchwell E., Walmsley M., eds, *IAU Symposium Vol. 227, Massive Star Birth: A Crossroads of Astrophysics*. pp 352–357 ([arXiv:astro-ph/0507705](https://arxiv.org/abs/astro-ph/0507705)), doi:10.1017/S1743921305004734
- Anderson L. D., et al., 2019, *ApJ*, **882**, 11
- Astropy Collaboration et al., 2013, *A&A*, **558**, A33
- Bailer-Jones C. A. L., Rybizki J., Fournesneau M., Mantelet G., Andrae R., 2018, *AJ*, **156**, 58
- Biegging J. H., Patel S., Peters W. L., Toth L. V., Marton G., Zahorecz S., 2016, *ApJS*, **226**, 13
- Burns R. A., et al., 2019, *PASJ*, **71**, 91
- Camargo D., Bonatto C., Bica E., 2011, *MNRAS*, **416**, 1522
- Cardelli J. A., Clayton G. C., Mathis J. S., 1989, *ApJ*, **345**, 245
- Chavarría L., Allen L., Brunt C., Hora J. L., Muench A., Fazio G., 2014, *MNRAS*, **439**, 3719
- Condon J. J., Cotton W. D., Greisen E. W., Yin Q. F., Perley R. A., Taylor G. B., Broderick J. J., 1998, *AJ*, **115**, 1693
- Courtès G., 1960, *Annales d'Astrophysique*, **23**, 115
- Dewangan L. K., Anandarao B. G., 2011, *MNRAS*, **414**, 1526
- Doi Y., et al., 2015, *PASJ*, **67**, 50
- Esteban C., García-Rojas J., 2018, *MNRAS*, **478**, 2315
- Evans II N. J., Blair G. N., 1981, *ApJ*, **246**, 394
- Gaia Collaboration et al., 2016, *A&A*, **595**, A1
- Gaia Collaboration et al., 2018, *A&A*, **616**, A1
- Georgelin Y. M., Georgelin Y. P., Roux S., 1973, *A&A*, **25**, 337
- Habing H. J., 1968, *Bull. Astron. Inst. Netherlands*, **19**, 421
- Heyer M. H., Carpenter J. M., Ladd E. F., 1996, *ApJ*, **463**, 630
- Hildebrand R. H., 1983, *QJRAS*, **24**, 267
- Hunter J. D., 2007, *Computing in Science & Engineering*, **9**, 90
- Hunter D. A., Massey P., 1990, *AJ*, **99**, 846
- Israel F. P., Felli M., 1978, *A&A*, **63**, 325
- Jones D. H., Shopbell P. L., Bland-Hawthorn J., 2002, *MNRAS*, **329**, 759
- Kaneda H., Kim W., Onaka T., Wada T., Ita Y., Sakon I., Takagi T., 2007, *PASJ*, **59**, S423
- Kartasheva T. A., Chunakova N. M., 1978, *Astrofizicheskie Issledovaniia Izvestiya Spetsial'noj Astrofizicheskoi Observatorii*, **10**, 44
- Kawada M., et al., 2007, *PASJ*, **59**, S389
- Keel W. C., et al., 2019, *MNRAS*, **483**, 4847
- Kim S.-H., Martin P. G., Hendry P. D., 1994, *ApJ*, **422**, 164
- Kirsanova M. S., Sobolev A. M., Thomasson M., Wiebe D. S., Johansson L. E. B., Seleznev A. F., 2008, *MNRAS*, **388**, 729
- Kirsanova M. S., Wiebe D. S., Sobolev A. M., Henkel C., Tsivilev A. P., 2014, *MNRAS*, **437**, 1593
- Klein R., Posselt B., Schreyer K., Forbrich J., Henning T., 2005, *ApJS*, **161**, 361
- Ladeyschikov D. A., Kirsanova M. S., Tsivilev A. P., Sobolev A. M., 2016, *Astrophysical Bulletin*, **71**, 208
- Lafon G., Deharveng L., Baudry A., de La Noë J., 1983, *A&A*, **124**, 1
- Lang D., Hogg D. W., Mierle K., Blanton M., Roweis S., 2010, *AJ*, **139**, 1782
- Mangum J. G., Shirley Y. L., 2015, *PASP*, **127**, 266
- Moiseev A. V., Egorov O. V., 2008, *Astrophysical Bulletin*, **63**, 181
- Moiseev A. V., Perepelitsyn A. E., Oparin D. V., 2020, *arXiv e-prints*, p. [arXiv:2005.14598](https://arxiv.org/abs/2005.14598)
- Murakami H., et al., 2007, *PASJ*, **59**, S369
- Ossenkopf V., Henning T., 1994, *A&A*, **291**, 943
- Osterbrock D. E., Ferland G. J., 2006, *Astrophysics of gaseous nebulae and active galactic nuclei*. Sausalito, CA: University Science Books
- Planck Collaboration et al., 2014, *A&A*, **571**, A11
- Price-Whelan A. M., et al., 2018, *AJ*, **156**, 123
- Proxauf B., Öttl S., Kimeswenger S., 2014, *A&A*, **561**, A10
- Quiroza C., Rood R. T., Balser D. S., Bania T. M., 2006a, *ApJS*, **165**, 338
- Quiroza C., Rood R. T., Bania T. M., Balser D. S., Maciel W. J., 2006b, *ApJ*, **653**, 1226
- Robitaille T., Bressert E., 2012, *APLpy: Astronomical Plotting Library in Python* (ascl:1208.017)
- Sharpless S., 1959, *ApJS*, **4**, 257
- Silverglate P. R., Terzian Y., 1978, *ApJ*, **224**, 437
- Straizys V., Drew J. E., Laugalys V., 2010, *Baltic Astronomy*, **19**, 169
- Takita S., et al., 2015, *PASJ*, **67**, 51
- Tielens A. G. G. M., 2005, *The Physics and Chemistry of the Interstellar Medium*. UK: Cambridge University Press
- Ueta T., Szczerba R., Fullard A. G., Takita S., 2019, *PASJ*, **71**, 5
- Wakelam V., Herbst E., 2008, *ApJ*, **680**, 371
- Weingartner J. C., Draine B. T., 2001, *ApJ*, **548**, 296
- Wenger M., et al., 2000, *A&AS*, **143**, 9
- Zhou S., Jaffe D. T., Howe J. E., Geis N., Herrmann F., Madden S. C., Poglitsch A., Stacey G. J., 1993, *ApJ*, **419**, 190

⁵ <http://www.astropy.org>

APPENDIX A: UNCERTAINTIES OF THE OBTAINED RESULTS

In this section we provide the reader with maps of signal to noise ratio. We show the ratio for the obtained emission line maps with original binning. We obtain comparable signal to noise ratio for the n_e and A_V values using 16 times larger pixel size than in the line emission maps.

This paper has been typeset from a $\text{\TeX}/\text{\LaTeX}$ file prepared by the author.

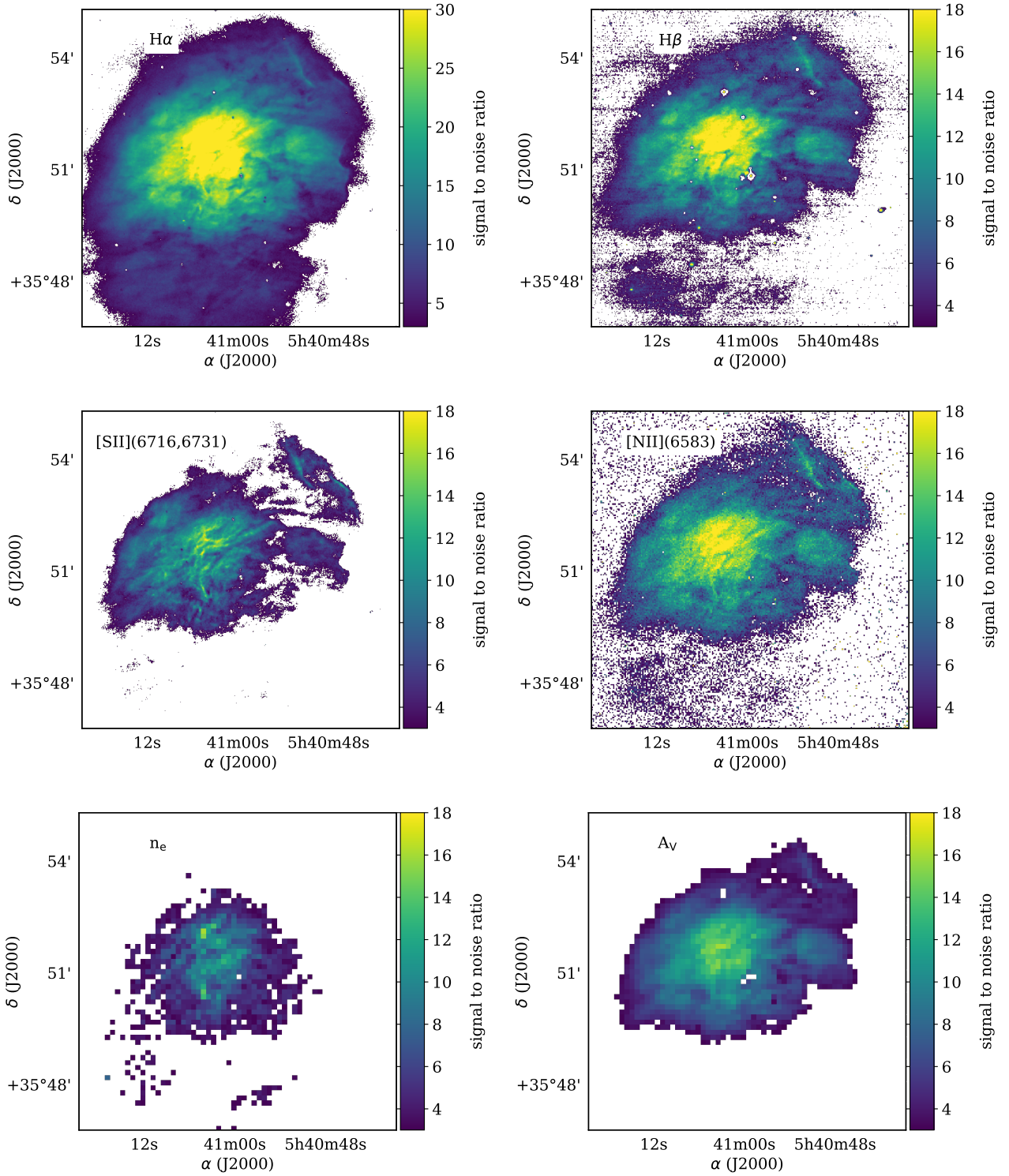


Figure A1. Maps of signal to noise ratio for pixels where the ratio is higher than 3. These pixels were used in the data analysis described in the paper.